Crystallization of classical multicomponent plasmas

Zach Medin* and Andrew Cumming†
Department of Physics, McGill University, 3600 Rue University, Montreal, Quebec, Canada H3A 2T8
(Received 15 December 2009; published 17 March 2010)

We develop a method for calculating the equilibrium properties of the liquid-solid phase transition in a classical, ideal, multicomponent plasma. Our method is a semianalytic calculation that relies on extending the accurate fitting formulas available for the one-, two-, and three-component plasmas to the case of a plasma with an arbitrary number of components. We compare our results to those of C. J. Horowitz *et al.* [Phys. Rev. E **75**, 066101 (2007)], who used a molecular-dynamics simulation to study the chemical properties of a 17-species mixture relevant to the ocean-crust boundary of an accreting neutron star at the point where half the mixture has solidified. Given the same initial composition as Horowitz *et al.*, we are able to reproduce to good accuracy both the liquid and solid compositions at the half-freezing point; we find abundances for most species within 10% of the simulation values. Our method allows the phase diagram of complex mixtures to be explored more thoroughly than possible with numerical simulations. We briefly discuss the implications for the nature of the liquid-solid boundary in accreting neutron stars.

DOI: 10.1103/PhysRevE.81.036107 PACS number(s): 89.90.+n, 97.60.Jd, 26.60.−c, 97.80.Jp

I. INTRODUCTION

During the crystallization of a plasma containing multiple ion species, the chemical composition of the solid is in general different from that of the liquid. This type of chemical separation is important for both white dwarfs [1] and accreting neutron stars [2]. The interior of a white dwarf is a mixture of carbon, oxygen, and traces of other elements, most abundantly neon. As the star cools, chemical separation leads to the formation of an oxygen- and neon-rich core. The energy released through the gravitational settling of the denser core material heats the star and can delay cooling by several Gyr [3]. A neutron star accretes mostly hydrogen and helium from its companion, but this material undergoes a series of nuclear reactions, including rapid proton capture [4] and then electron-capture reactions [5], to produce a variety of elements. Through accretion, the mixture is pushed deep into the star and solidifies. Recent numerical simulations have shown that the mixture undergoes chemical separation during solidification [2], possibly forming a two-phase solid [6]. The composition of the liquid ocean and the structure and composition of the crust have important implications for a range of observed phenomena. For example, the resulting thermal conductivity determines the cooling rate of transiently accreting neutron stars following extended accretion outbursts [7,8]. The mechanical strength of the crust limits the size of a possible crust quadrupole and therefore gravitational wave emission [9].

Several groups have studied the liquid-solid phase transition and chemical separation of two- and three-component plasmas in the classical, ideal limit (i.e., ignoring quantum-mechanical effects on the ions and treating the electrons as a uniform background; cf. Ref. [10]). Early works (e.g., Ref. [11]) studied phase transitions in carbon-oxygen plasmas, but the approximations used were too crude for application to the interiors of white dwarfs. Accurate calculations using the mean spherical approximation in the density-functional formalism were performed by Barrat *et al.* [12], who studied carbon-oxygen plasmas, and by Segretain and Chabrier [13], who studied arbitrary two-component plasmas with atomic number Z ratios up to 2 (see also Ref. [14], where carbon-oxygen-neon plasmas are examined). Using Monte Carlo calculations and Z ratios up to 5, Ogata *et al.* [15] studied arbitrary two- and three-component plasmas and DeWitt and Slattery [16] two-component plasmas with a very accurate measurement of the liquid free energy (see also Refs. [17,18]). All of these groups present phase diagrams as a function of ion abundance and some [15,16] also present fitting formulas for the liquid and solid free energies. Using these diagrams and fitting formulas, one can determine the phase-transition properties for a two-component plasma of any ion type and abundance.

These calculations are particularly useful for the interior of a white dwarf, where there are only two or three dominant elements. But in the ocean of an accreting neutron star, there are around 10–20 elements with abundances $>1\%$ [5], each one with a potentially important effect on the behavior of the phase transition and chemical separation of the mixture. The available analytic or numerical results for this type of system are extremely limited. We are aware of only one study of phase transitions in plasmas with more than three components: that of Horowitz *et al.* [2] (see also Refs. [6,19]). These authors used molecular-dynamics simulations to study a 17-component plasma with a composition similar to that expected at the ocean-crust interface of an accreting neutron star. Due to the large amount of computing power necessary to run each simulation, the phase-transition properties have so far only been calculated for one composition.

We present here a method for rapidly calculating the properties of the liquid-solid phase transition in a multicomponent plasma in the classical ideal limit for any initial composition and ion types. Our method is a semianalytic calculation that relies on extending the accurate fitting formulas available for the one-, two-, and three-component plasmas to the case of a plasma with an arbitrary number of

*zmedin@physics.mcgill.ca
†cumming@physics.mcgill.ca

components. We test our method using the one data point available for a plasma with more than three components, the calculation of [2], and show that it performs very well in that specific case.

The paper is organized as follows. In Sec. II we describe the semianalytic calculation as it applies to the one-component plasma (Sec. II A), the two-component plasma (Sec. II B), and the multicomponent plasma (Sec. II C). In Sec. III, we present our results for the 17-component mixture of Horowitz *et al.* [2]. We conclude in Sec. IV. The pressure term in the Gibbs free energy and its effect on the phase transition, the importance of the deviation from linear mixing for the liquid free energy, and a simplified derivation of the deviation from linear mixing for the solid free energy are discussed in Appendixes A–C.

II. METHOD

A. One-component plasma

We assume in this paper that the system has reached equilibrium, i.e., the state of lowest free energy. The validity of this assumption and nonequilibrium effects such as diffusion and sedimentation will be discussed in a later paper. We also assume here that the phase transition happens at constant volume, in which case the equilibrium configuration of the system is determined by the state with the lowest Helmholtz free energy, $F=U-TS$. In reality, the transition happens at constant pressure and at minimized Gibbs free energy. The error introduced by using the constant volume approximation is discussed in Appendix A. We find that for the mixture considered in Sec. III, the abundance in the liquid state of each ion species is in error by no more than 2%. While the percentage errors in the abundances in the solid state are typically larger by factors of ~2–5, the absolute errors for each ion species are similar in either state. (Since this trend holds true for most of the approximations we make in this paper, we hereafter quote errors in our approximations only for the liquid abundances.) Note that in transitions at constant volume, the free energy of the electrons is identical in the liquid and in the solid and so has no effect on the properties of the phase transition.

The Helmholtz free energy of the liquid or solid phase of a one-component plasma (OCP) can be described as a function of only the number of ions N, the temperature T, and the Coulomb coupling parameter $\Gamma \equiv (Ze)^2/(ak_BT) = Z^{5/3}\Gamma_e$. Here, Ze is the ion charge, a is the ion separation, and k_B is the Boltzmann constant; $\Gamma_e \equiv e^2/(a_e k_B T)$ is the electron coupling parameter, where $a_e = [3/(4\pi n_e)]^{1/3}$ is the mean electron spacing and $n_e = ZN/V$ is the electron density.

The ideal-gas contribution to the free energy of a one-component plasma F_{ideal} is given by

$$f_{\text{ideal}} \equiv \frac{F_{\text{ideal}}}{Nk_BT} = \ln\left[\frac{N}{V}\left(\frac{h^2}{2\pi m_i k_B T}\right)^{3/2}\right] - 1$$

$$= 3\ln\Gamma + \frac{3}{2}\ln(k_BT)_{\text{Ry}} - 1 - \ln\frac{4}{3\sqrt{\pi}}, \quad (1)$$

where $m_i = Am_p$ is the mass of the ion and $(k_BT)_{\text{Ry}} = k_BT 2\hbar^2/(m_i Z^4 e^4)$ is the thermal energy expressed in ionic Rydberg units. The free energy of the liquid phase of a one-component plasma F_l^{OCP} is well fit for $\Gamma \in [1, 200]$ by

$$f_l^{\text{OCP}}(\Gamma) \equiv \frac{F_l^{\text{OCP}}}{Nk_BT} = -0.899\,172\Gamma + 1.8645\Gamma^{0.323\,01}$$

$$- 0.2748\ln(\Gamma) - 1.4019. \quad (2)$$

The previous formula is from the Monte Carlo calculations of DeWitt and Slattery [16], with the modification that the ideal-gas contribution to the free energy [Eq. (1)] has been removed. Other formulas for f_l^{OCP} can be found in Refs. [10,20–22] (see also Refs. [23,24]); for the range of Γ we are concerned with in this paper ($15 \lesssim \Gamma \lesssim 200$), the differences between these formulas, and between the numerical data these formulas are based on, are less than 0.006.

The free energy of the solid phase of a one-component plasma F_s^{OCP} is well fit for $\Gamma \in [160, 2000]$ by

$$\frac{F_s^{\text{OCP}}}{Nk_BT} = -0.895\,929\Gamma + 1.5\ln(\Gamma) - 1.1703$$

$$- \frac{10.84}{\Gamma} - \frac{176.4}{\Gamma^2} - \frac{5.980\times 10^4}{\Gamma^3}. \quad (3)$$

The previous formula is from [25]; it was derived using a combination of analytic methods and a fit to the Monte Carlo calculations of Ref. [26]. As in the liquid case, we have modified Eq. (3) from its original form by removing the ideal-gas contribution. Another formula for $F_s^{\text{OCP}}/(Nk_BT)$ of similar accuracy (with less than 0.004 difference from Ref. [25] or the numerical data for $160 \le \Gamma \le 2000$) can be obtained from the molecular-dynamics calculations of Ref. [24] (see also Refs. [20,27]). In this paper, we neglect the Γ^{-2} and Γ^{-3} terms in Eq. (3) and use the following approximation for F_s^{OCP}:

$$f_s(\Gamma)^{\text{OCP}} \equiv \frac{F_s^{\text{OCP}}}{Nk_BT} \simeq -0.895\,929\Gamma + 1.5\ln(\Gamma)$$

$$- 1.1703 - \frac{10.84}{\Gamma}. \quad (4)$$

This expression fits the numerical data for $160 \le \Gamma \lesssim 300$ with an accuracy several times lower than that of Eq. (3) (differing by up to 0.02 for $\Gamma \sim 160$). We use this expression in place of Eq. (3), however, because it behaves qualitatively better for small Γ, as we discuss below.

The free-energy difference based on these fits is given by

$$\delta f_{\text{fit}}^{\text{OCP}}(\Gamma) \equiv (f_l - f_s)^{\text{OCP}} = -0.003\,243\Gamma + 1.8645\Gamma^{0.32301}$$

$$- 1.7748\ln(\Gamma) - 0.2316 + 10.84/\Gamma. \quad (5)$$

In equilibrium, the system will be in the state of lowest free energy: when $\delta f^{\text{OCP}} < 0$, the OCP is in the liquid state, and when $\delta f^{\text{OCP}} > 0$, it is in the solid state. When $\delta f^{\text{OCP}} = 0$, there is a phase transition between the liquid and solid state. This occurs at

$$\Gamma_{\rm crit} = 178.6 \tag{6}$$

in the above equation. Note that if we had used Eq. (3) instead of Eq. (4) to calculate $\delta f_{\rm fit}^{\rm OCP}$, we would obtain $\Gamma_{\rm crit}=175.3$, which is in agreement with the most accurate estimates currently available for this value (e.g., $\Gamma_{\rm crit}=175.0\pm0.4$ in Ref. [10]); our $\Gamma_{\rm crit}$ differs from the true transition value by about 2%.

Equation (5) is only accurate for $\Gamma\in[160,200]$. While there are no Monte Carlo or molecular-dynamics data available for $f_l^{\rm OCP}$ when $\Gamma>200$, Ichimaru *et al.* [28] calculated $f_l^{\rm OCP}$ up to $\Gamma=1000$ using the "improved hypernetted chain" (IHNC) method. For $\Gamma\in[200,1000]$, if $f_l^{\rm OCP}$ is given by Ref. [28] and $f_s^{\rm OCP}$ is given by Eq. (4), the approximation

$$\delta f^{\rm OCP}(\Gamma) = 0.09 + 0.0043(\Gamma - 200) \tag{7}$$

fits the free-energy difference to within 0.2. This error is of similar magnitude to the error in the IHNC method for $\Gamma>200$ (as extrapolated from comparisons between IHNC approximations and Monte Carlo calculations at $\Gamma<200$; see, e.g., [29,30]), and is several times smaller than the error that would be obtained by a direct application of Eq. (5) to the domain $\Gamma\in[200,1000]$.

There are currently no published results (numerical or otherwise) for $f_l^{\rm OCP}$ above $\Gamma=1000$ or $f_s^{\rm OCP}$ below $\Gamma=160$. However, we expect $\delta f^{\rm OCP}$ to increase monotonically with increasing Γ, not just in [160, 1000] but for all Γ. In other words, for the OCP, the solid state should always become more stable with respect to the liquid as Γ increases and less stable as Γ decreases. Equation (7) extended out to arbitrarily large Γ remains consistent with this assumption, but Eq. (5) extended down to $\Gamma=0$ does not. This is because $\delta f_{\rm fit}^{\rm OCP}$ decreases with Γ for $\Gamma\in[0,50]$. An even stronger argument against $\delta f_{\rm fit}^{\rm OCP}$ representing the true free-energy difference at small Γ is that $\delta f_{\rm fit}^{\rm OCP}>0$ for $\Gamma<17$, which would imply that the OCP were in the solid state at very low Γ. Note that these effects are even worse if Eq. (3) is used to represent $f_s^{\rm OCP}$: in that case, the free-energy difference decreases with Γ for $\Gamma\in[0,85]$ and is greater than zero for $\Gamma<51$. To avoid small-Γ problems, we cut off Eq. (5) at $\Gamma=100$ and assume that below this value, the free-energy difference is given by

$$\delta f^{\rm OCP}(\Gamma) = -0.37 + 0.0046(\Gamma - 100), \tag{8}$$

i.e., by the line tangent to $\delta f_{\rm fit}^{\rm OCP}$ at $\Gamma=100$. If we had instead used Eq. (3) to represent $f_s^{\rm OCP}$ in $\delta f_{\rm fit}^{\rm OCP}$, Eq. (8) would change to $\delta f^{\rm OCP}(\Gamma)=-0.30+0.0025(\Gamma-100)$. Such a change leads to "errors" in the multicomponent results (Secs. II B and II C) of no more than 5% for the liquid abundances, comparable to what is seen in Fig. 5.

Our final expression for $\delta f^{\rm OCP}$, valid over all Γ, is

$$\delta f^{\rm OCP}(\Gamma) = \begin{cases} \delta f_{\rm fit}^{\rm OCP}(\Gamma), & 100<\Gamma<200 \\ -0.37+0.0046(\Gamma-100), & \Gamma<100 \\ 0.09+0.0043(\Gamma-200), & \Gamma>200, \end{cases} \tag{9}$$

where $\delta f_{\rm fit}^{\rm OCP}(\Gamma)$ is given by Eq. (5).

B. Two-component plasma

The free energy of a two-component plasma (TCP) can be described as a function of N, T, and the Coulomb coupling parameter $\Gamma_i=Z_i^{5/3}\Gamma_e$ and fractional composition $x_i=N_i/N$ of either species of ion. Here, $N=N_1+N_2$ is the total number of ions and $n_e=(Z_1N_1+Z_2N_2)/V$ is the total electron density. For the rest of this section, we will identify the composition of the TCP by x_1 and the Coulomb coupling parameter by Γ_1, since we can express x_2 and Γ_2 as functions of these values: $x_2=1-x_1$ and $\Gamma_2=(Z_2/Z_1)^{5/3}\Gamma_1$. Note that throughout this paper, we choose to label the ionic species such that $Z_1<Z_2<\cdots<Z_m$, where m is the total number of species; Z_1 always represents the ion with the smallest charge.

The free energy of the liquid phase of a two-component plasma is given by

$$f_l^{\rm TCP}(\Gamma_1,x_1) = \sum_{i=1}^{2} x_i\left[f_l^{\rm OCP}(\Gamma_i) + \ln\left(x_i\frac{Z_i}{\langle Z\rangle}\right)\right] + \Delta f_l(\Gamma_1,x_1), \tag{10}$$

where $\langle Z\rangle=\Sigma_{i=1}^2 x_iZ_i$ is the average ion charge. The $\Sigma_{i=1}^2 x_i\ln(x_i\frac{Z_i}{\langle Z\rangle})$ term is the (ideal-gas) entropy of mixing for two species of volumes Z_1N_1/n_e and Z_2N_2/n_e, and Δf_l is the deviation from linear mixing in the liquid. The deviation term Δf_l has a similar dependence on x_i to the entropy of mixing term, but is in general much smaller in magnitude (see, e.g., Refs. [15,18,31]). We therefore expect this deviation to have a minimal effect on the phase-transition properties for most systems. In our calculation, we set $\Delta f_l=0$ and use the linear mixing approximation

$$f_l^{\rm TCP}(\Gamma_1,x_1) \simeq \sum_{i=1}^{2} x_i\left[f_l^{\rm OCP}(\Gamma_i) + \ln\left(x_i\frac{Z_i}{\langle Z\rangle}\right)\right]. \tag{11}$$

The error introduced by neglecting the Δf_l term in the expression for $f_l^{\rm TCP}$ is discussed in Appendix B.

The free energy of the solid phase of a two-component plasma is given by

$$f_s^{\rm TCP}(\Gamma_1,x_1) = \sum_{i=1}^{2} x_i\left[f_s^{\rm OCP}(\Gamma_i) + \ln\left(x_i\frac{Z_i}{\langle Z\rangle}\right)\right] + \Delta f_s(\Gamma_1,x_1), \tag{12}$$

where Δf_s is the deviation from linear mixing in the solid. Unlike Δf_l, which is generally small even at large Γ_1 (Appendix B), Δf_s is comparable to the other terms in f_s and grows linearly with Γ_1; we therefore expect Δf_s to play an important role in setting the phase-transition properties. For charge ratios $R_Z=Z_2/Z_1$ in the range $R_Z\in[1:5]$, the deviation is well fit by

$$\Delta f_s(\Gamma_1,x_1) \simeq \Gamma_1x_1x_2\Delta g(x_2,Z_2/Z_1), \tag{13}$$

where

$$\Delta g(x,R_Z) = \frac{C(R_Z)}{1+\frac{27(R_Z-1)}{1+0.1(R_Z-1)}\sqrt{x}(\sqrt{x}-0.3)(\sqrt{x}-0.7)(\sqrt{x}-1)}, \tag{14}$$

$$C(R_Z) = \frac{0.05(R_Z-1)^2}{[1+0.64(R_Z-1)][1+0.5(R_Z-1)^2]}. \tag{15}$$

Equation (13) is from the Monte Carlo calculations of [15] and is accurate to within 10% for $R_Z \lesssim 4.5$; a similar formula (though accurate only for $R_Z \lesssim 2$) can be found in [16]. To estimate the error introduced to our results by adopting Eq. (13), we run several calculations with a deviation of $1.1\Delta f_s(\Gamma_1,x_1)$ and $0.9\Delta f_s(\Gamma_1,x_1)$ [i.e., 10% higher or lower than the deviation we use in our model]. For the TCP, we find errors in the liquid abundances of 5% or less, with the largest errors at high Γ values and moderate charge ratios ($R_Z \sim 1.5$). For the 17-component mixture and Γ value considered in Sec. III, the errors in the liquid abundances are only 2% or less.

For a TCP at a particular value of Γ_1, we find the state of lowest free energy as a function of composition by using the "double-tangent" construction (see, e.g., Ref. [32]). We construct lines tangent to the minimum free energy curve $f_{\min} = \min(f_l, f_s)$ in at least two points, corresponding to the compositions a_1 and b_1; an example of this construction is shown graphically in Fig. 1. Any homogeneous composition x_1 that lies between a_1 and b_1, i.e., any x_1 which can be expressed as $Aa_1+(1-A)b_1=x_1$ for some $0<A<1$, satisfies $Af_{\min}(a_1)+(1-A)f_{\min}(b_1)<f_{\min}(x_1)$ and is therefore unstable with respect to a heterogeneous mixture of a_1 and b_1. In this paper, we refer to the locus of all points (Γ_1,x_1) that lie between double-tangent points (Γ_1,a_1) and (Γ_1,b_1) as the "unstable region" of the phase diagram.

Note that double-tangent points a_1 and b_1 can potentially be constructed from the liquid curve to itself, from the solid curve to itself, or from the liquid curve to the solid curve, depending on the behavior of f_l and f_s [see Eqs. (11) and (12)]. In some cases, "triple-tangent" points can be constructed; typically, this occurs when the solid curve is tangent to itself and to the liquid curve (when the liquid is at the "eutectic point;" see, e.g., Ref. [13]). The liquid-solid solutions are discussed below in Sec. IIB1. In the approximation we have adopted above, where the deviation from linear mixing for the liquid is $\Delta f_l=0$, tangents to the liquid curve f_l do not intersect the curve at any other point [cf. Eq. (11)]; therefore, there are no liquid-liquid solutions. Because of the $\Delta f_s>0$ term in the solid curve, which grows proportional with Γ_1 [see Eq. (13)], when Γ_1 is large enough, there will always be regions of f_s where double tangents can be constructed from the solid curve to itself. These solid-solid solutions will be examined in a later paper.

Solving for the liquid-solid equilibrium of the two-component plasma

For a two-component plasma, liquid-solid phase transitions occur at compositions and Γ values where double-tangent lines can be drawn connecting the free-energy curves of the liquid and the solid. Under these conditions, a liquid state of composition a_1 and a solid state of composition b_1 exist simultaneously as a mixture. For a double-tangent line connecting f_l to f_s, the line must satisfy

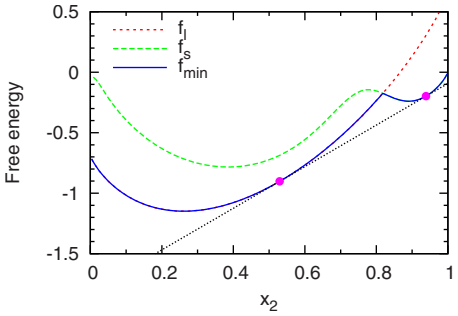

FIG. 1. (Color online) An example of the double-tangent construction for $R_Z=34/8$ and $\Gamma_1=\Gamma_{\rm crit}/6$ (cf. Figs. 4 and 5). The stable compositions a_2 and b_2 (i.e., $1-a_1$ and $1-b_1$) are marked by filled circles; here, one of the mixtures is stable in the liquid state and one is stable in the solid state. Note that the curves f_l and f_s plotted in this figure are given not by Eqs. (11) and (12), respectively, but by these equations minus the term $\Sigma_{i=1}^{2} x_i f_l^{\rm OCP}(\Gamma_i)$. The values of a_2 and b_2 obtained are the same whether $f_l^{\rm TCP}$ and $f_s^{\rm TCP}$ or these modified expressions are used: adding terms constant or linear in the x_i's to both free-energy curves has no effect on the results of the double-tangent construction.

$$f_l'(a_1) = f_s'(b_1) \tag{16}$$

and

$$f_l(a_1) + (b_1-a_1)f_l'(a_1) = f_s(b_1). \tag{17}$$

For later convenience, we rewrite these equations as

$$f_l(a_1) + (1-a_1)f_l'(a_1) = f_s(b_1) + (1-b_1)f_s'(b_1) \tag{18}$$

and

$$f_l(a_1) - a_1 f_l'(a_1) = f_s(b_1) - b_1 f_s'(b_1). \tag{19}$$

Using Eqs. (11) and (12), the system of equations to solve becomes

$$\delta f^{\rm OCP}(\Gamma_1) + \ln\left(a_1\frac{Z_1}{\langle Z\rangle^a}\right) - \frac{Z_1}{\langle Z\rangle^a} = \ln\left(b_1\frac{Z_1}{\langle Z\rangle^b}\right) - \frac{Z_1}{\langle Z\rangle^b} - \Delta f_s + \Gamma_1 b_2\left\{\Delta g(b_2,Z_2/Z_1) - b_1 b_2\left[\frac{d\Delta g}{dx}\right](b_2,Z_2/Z_1)\right\}, \tag{20}$$

$$\delta f^{\rm OCP}(\Gamma_2) + \ln\left(a_2\frac{Z_2}{\langle Z\rangle^a}\right) - \frac{Z_2}{\langle Z\rangle^a} = \ln\left(b_2\frac{Z_2}{\langle Z\rangle^b}\right) - \frac{Z_2}{\langle Z\rangle^b} - \Delta f_s + \Gamma_1 b_1\left\{\Delta g(b_2,Z_2/Z_1) - b_1 b_2\left[\frac{d\Delta g}{dx}\right](b_2,Z_2/Z_1)\right\}, \tag{21}$$

where $\langle Z\rangle_a=\Sigma a_i Z_i$, $\langle Z\rangle_b=\Sigma b_i Z_i$, and

$$\left[\frac{d\Delta g}{dx}\right](x,R_Z)=-\frac{C(R_Z)(2x-3\sqrt{x}+1.21-0.105/\sqrt{x})}{\left[1+\frac{27(R_Z-1)}{1+0.1(R_Z-1)}\sqrt{x}(\sqrt{x}-0.3)(\sqrt{x}-0.7)(\sqrt{x}-1)\right]^2}. \tag{22}$$

[cf. Eq. (14)]. With these two equations (and $a_1+a_2=1$, $b_1+b_2=1$), if we are given Γ_1, we can solve for a_1 and b_1. This allows us to trace out the liquid-solid unstable region of the phase diagram for Γ_1 versus x_1. Note that to map out the full phase diagram, we also need to know the shape of the solid-solid unstable region; this is most important at large Γ_1. Examples of phase diagrams for TCPs (including both types of unstable regions) are shown in Appendixes A–C.

C. Multicomponent plasma

The free energy of an m-component plasma (MCP) can be described as a function of N, T, the fraction composition of each ion species $x_i=N_i/N$ (though x_m is not needed, since $x_m=1-\Sigma x_i$), and the Coulomb coupling parameter of one ion species. In the following, we solve for $\Gamma_1=Z_1^{5/3}\Gamma_e$ and then use the relation $\Gamma_i=(Z_i/Z_1)^{5/3}\Gamma_1$ to find the other parameters.

As with the two-component plasma, the free energy of the liquid phase of a multicomponent plasma is very well described by the linear mixing rule (but see Appendix B)

$$f_l^{\mathrm{MCP}}(\Gamma_1,x_1,\ldots,x_{m-1})\simeq\sum_{i=1}^{m}x_i\left[f_l^{\mathrm{OCP}}(\Gamma_i)+\ln\left(x_i\frac{Z_i}{\langle Z\rangle}\right)\right], \tag{23}$$

where $\langle Z\rangle=\Sigma_{i=1}^{m}x_iZ_i$.

The free energy of the solid phase of the MCP is

$$f_s^{\mathrm{MCP}}(\Gamma_1,x_1,\ldots,x_{m-1})\simeq\sum_{i=1}^{m}x_i\left[f_s^{\mathrm{OCP}}(\Gamma_i)+\ln\left(x_i\frac{Z_i}{\langle Z\rangle}\right)\right]+\Delta f_s(\Gamma_1,x_1,\ldots,x_{m-1}). \tag{24}$$

According to [15], the deviation of the solid from linear mixing Δf_s for a three-component plasma is given to good accuracy by

$$\Delta f_s(\Gamma_1,x_1,\ldots,x_{m-1})\simeq\sum_{i=1}^{m-1}\sum_{j=i+1}^{m}\Gamma_i x_i x_j\Delta g\left(\frac{x_j}{x_i+x_j},\frac{Z_j}{Z_i}\right), \tag{25}$$

where $Z_1<Z_2<\cdots<Z_m$ and $\Delta g(x,R_Z)$ is given by Eq. (14). We assume here that Eq. (25) applies for all $m\geq 2$. A partial justification for this assumption is provided in Appendix C.

In the m-component plasma, we construct $(m-1)$-dimensional hyperplanes tangent to the minimum free-energy surface in at least two points, corresponding to the compositions $\vec{a}$ and $\vec{b}$. Any homogeneous composition $\vec{x}$ that lies between $\vec{a}$ and $\vec{b}$, i.e., any $\vec{x}$ which can be expressed as $A\vec{a}+(1-A)\vec{b}=\vec{x}$ for some $0<A<1$, is unstable with respect to a heterogeneous mixture of $\vec{a}$ and $\vec{b}$.

Solving for the liquid-solid equilibrium of the multicomponent plasma

For a multicomponent plasma, liquid-solid phase transitions occur at compositions and Γ values where double-tangent hyperplanes can be drawn connecting the free-energy surfaces of the liquid and the solid. For a double-tangent hyperplane connecting $f_l(\vec{a})$ to $f_s(\vec{b})$, the hyperplane must satisfy

$$\frac{df_l}{dx_i}(\vec{a})=\frac{df_s}{dx_i}(\vec{b}),\quad i\in[1,m-1] \tag{26}$$

and

$$f_l(\vec{a})+(\vec{b}-\vec{a})\cdot\vec{\nabla}f_l(\vec{a})=f_s(\vec{b}), \tag{27}$$

or

$$f_l(\vec{a})+\frac{df_l}{dx_i}(\vec{a})-\vec{a}\cdot\vec{\nabla}f_l(\vec{a})=f_s(\vec{b})+\frac{df_s}{dx_i}(\vec{b})-\vec{b}\cdot\vec{\nabla}f_s(\vec{b}),\quad i\in[1,m-1] \tag{28}$$

and

$$f_l(\vec{a})-\vec{a}\cdot\vec{\nabla}f_l(\vec{a})=f_s(\vec{b})-\vec{b}\cdot\vec{\nabla}f_s(\vec{b}). \tag{29}$$

Using Eqs. (23) and (24), the system of equations to solve becomes

$$\begin{aligned}\delta f^{\mathrm{OCP}}(\Gamma_i)+\ln\left(a_i\frac{Z_i}{\langle Z\rangle_a}\right)-\frac{Z_i}{\langle Z\rangle_a}&=\ln\left(b_i\frac{Z_i}{\langle Z\rangle_b}\right)-\frac{Z_i}{\langle Z\rangle_b}-\Delta f_s(\Gamma_1,x_1,\ldots,x_{m-1})\\&+\sum_{j=1}^{i-1}\Gamma_j b_j\left\{\Delta g\left(\frac{b_i}{b_i+b_j},\frac{Z_i}{Z_j}\right)+\frac{b_ib_j}{(b_i+b_j)^2}\left[\frac{d\Delta g}{dx}\right]\times\left(\frac{b_i}{b_i+b_j},\frac{Z_i}{Z_j}\right)\right\}+\sum_{j=i+1}^{m}\Gamma_i b_j\left\{\Delta g\left(\frac{b_j}{b_i+b_j},\frac{Z_j}{Z_i}\right)\right.\\&\left.-\frac{b_ib_j}{(b_i+b_j)^2}\left[\frac{d\Delta g}{dx}\right]\left(\frac{b_j}{b_i+b_j},\frac{Z_j}{Z_i}\right)\right\}\end{aligned} \tag{30}$$

for $i\in[1,m]$. Here, $\langle Z\rangle_a=\Sigma a_iZ_i$, $\langle Z\rangle_b=\Sigma b_iZ_i$, and $[\frac{d\Delta v}{dx}](x,R_Z)$ is again given by Eq. (22). With these m equations (and $\Sigma a_i=1$, $\Sigma b_i=1$), if we are given the liquid com-

TABLE I. Abundance of chemical element Z for various mixtures from the numerical simulation of Horowitz *et al.* [2]. Abundances are provided for the initial mixture (in the column labeled "Initial") and the final liquid and solid mixtures (in the columns labeled "Liquid" and "Solid," respectively). For each final mixture, the average charge $\langle Z\rangle$ and Coulomb coupling parameter $\Gamma=\langle Z^{5/3}\rangle\Gamma_e$ are provided as well. The percentage error for each entry is given by $100/\sqrt{N_i}$, where $N_i=x_iN$ and $N=27\,648$.

HBB results $\langle Z\rangle_l=28.04$, $\langle Z\rangle_s=30.48$, $\Gamma_1=27.7$, $\Gamma_l=233$, $\Gamma_s=261$					
Z	Initial	Liquid	% Error	Solid	% Error
8	0.0301	0.0529	3	0.0087	6
10	0.0116	0.0205	4	0.0021	13
12	0.0023	0.0043	9	0.0006	24
14	0.0023	0.0043	9	0.0005	27
15	0.0023	0.0043	9	0.0004	30
20	0.0046	0.0055	8	0.0029	11
22	0.0810	0.1024	2	0.0616	2
24	0.0718	0.0816	2	0.0635	2
26	0.1019	0.1065	2	0.1017	2
27	0.0023	0.0025	12	0.0027	12
28	0.0764	0.0744	2	0.0746	2
30	0.0856	0.0773	2	0.0949	20
32	0.0116	0.0099	6	0.0130	5
33	0.1250	0.1079	2	0.1388	1
34	0.3866	0.3408	1	0.4297	0.9
36	0.0023	0.0012	17	0.0030	11
47	0.0023	0.0030	11	0.0013	17

position $\vec{a}$, we can solve for the solid composition $\vec{b}$ and Coulomb parameter Γ_1 at which the liquid and solid states are in equilibrium; if we are given $\vec{b}$, we can solve for $\vec{a}$ and Γ_1. In this manner, we can trace out the liquid-solid unstable region of the phase diagram for Γ_1 versus $\vec{x}$. As in the TCP case, to map out the full phase diagram, we also need to know the shape of the solid-solid unstable region.

Alternatively, if we are given an initial composition $\vec{x}$ and the fraction $0<A<1$ of the solution in the liquid state (or the fraction $1-A$ in the solid state), we can solve for Γ_1 and the compositions of both the liquid and solid mixtures in equilibrium. We have $2m-1$ unknowns, $a_1,\ldots,a_{m-1}$, $b_1,\ldots,b_{m-1}$, and Γ_1; but in addition to the m equations Eq. (30) above, we have the $m-1$ equations

$$Aa_i+(1-A)b_i=x_i,\quad i\in[1,m-1]. \tag{31}$$

III. RESULTS

As described in Sec. I, Horowitz, Berry, and Brown [2] (hereafter HBB) used a molecular-dynamics simulation to study the phase transition of a 17-component plasma. A total of 27 648 ions are placed in a simulation volume of length 727.5 fm on a side. At the start of the simulation, 50% of the plasma is in the liquid state and 50% is in the solid state. There is a uniform composition throughout the volume, given by the results of Gupta *et al.* [5] (who calculated the composition of an accreting neutron star at a density of 2×10^{11} g/cm^3 after the accreted material has undergone proton and electron capture and various other reactions). As the system evolves, the temperature is adjusted so that approximately half of the plasma remains in the liquid state and half remains in the solid state. After a simulation time of 5×10^6 fm/c, the simulation is run at constant energy until the total time reaches 151×10^6 fm/c. The results of the numerical simulation are shown in Table I. The final temperature of the simulation is expressed in terms of Γ_1 as well as the "average" Coulomb coupling parameter, $\Gamma=\langle Z^{5/3}\rangle\Gamma_e$. For each entry in Table I, a statistical ($\sqrt{N_i}$) error is provided.

We have applied our semianalytic calculation (Sec. II C) to the same 17-component mixture as is considered by HBB. In Eq. (31), we set $\vec{x}$ to the "initial" composition given in Table I and choose $A=0.5$, such that we are solving for the equilibrium state where 50% of the mixture is liquid and 50% is solid. We then use Eqs. (30) and (31) to find the final composition of the liquid and solid states, $\vec{a}$ and $\vec{b}$. The result is given in Table II. For each entry in Table II, an error is provided in terms of the percent difference from the corresponding HBB result.

The results of Table II are relevant under equilibrium conditions, which in the accreting neutron star means that the particles solidify and diffuse through the liquid and the solid faster than new material is accreted. Here we attempt to estimate the importance of the diffusion rate on the overall results. In order to do that, we repeat our calculation done

TABLE II. Abundance of chemical element Z for the liquid and solid mixtures from our equilibrium calculation. Here, instantaneous diffusion is assumed (see text). For each mixture, the average charge $\langle Z\rangle$ and Coulomb coupling parameter $\Gamma=\langle Z^{5/3}\rangle\Gamma_e$ are provided as well. The initial liquid mixture is given by its value from HBB and the system is evolved until there is 50% liquid material, 50% solid material. The percent error for each entry is given by $100\times$(entry−HBB)/HBB.

Instant diffusion $\langle Z\rangle_l=27.667$, $\langle Z\rangle_s=30.930$, $\Gamma_1=26.57$, $\Gamma_l=218.3$, $\Gamma_s=256.1$ (Γ_1 error: −4%)					
Z	Initial	Liquid	% Error	Solid	% Error
8	0.0301	0.0513	−3	0.0089	+3
10	0.0116	0.0197	−4	0.0035	+66
12	0.0023	0.0039	−8	0.0007	+10
14	0.0023	0.0040	−7	0.0006	+22
15	0.0023	0.0040	−7	0.0006	+54
20	0.0046	0.0073	+32	0.0019	−33
22	0.0810	0.1213	+18	0.0407	−34
24	0.0718	0.0947	+16	0.0489	−23
26	0.1019	0.1161	+9	0.0877	−14
27	0.0023	0.0024	−4	0.0022	−19
28	0.0764	0.0758	+2	0.0770	+3
30	0.0856	0.0759	−2	0.0953	+0.5
32	0.0116	0.0095	−4	0.0137	+5
33	0.1250	0.1013	−6	0.1487	+7
34	0.3866	0.3076	−10	0.4656	+8
36	0.0023	0.0018	−12	0.0028	−8
47	0.0023	0.0033	+9	0.0013	+2

with "instantaneous diffusion" (Table II), this time assuming "no diffusion" in the solid [36]. As in the equilibrium case, the calculation starts with the plasma in the liquid state with initial composition given by HBB and ends when 50% of the plasma is liquid and 50% is solid. Unlike in the equilibrium case, however, we solve Eqs. (30) and (31) many times, each time producing a small amount of solid material $(1-A\ll 1)$. Solid particles created in one step are removed from consideration in all future steps, since we are assuming that these particles do not mix. The liquid composition $(\vec{a})$ calculated in one step is used as the "initial" composition $(\vec{x})$ in the next step.

While an exact treatment of the no diffusion limit would require solving Eqs. (30) and (31) on a particle-to-particle basis, we find that a good approximation can be obtained using 500 steps with $A_k=1-1/(1001-k)$ for each step k. [The difference between the final abundances calculated using 50 steps with $A_k=1-1/(101-k)$ and 500 steps with $A_k=1-1/(1001-k)$, e.g., is less than 0.2%.] The result is given in Table III. Note that for this choice for A_k, the number of solid particles created is the same in each step. The average solid composition is given by

$$\langle\vec{b}\rangle=\frac{1}{50}\sum_{k=1}^{50}\vec{b}^k, \tag{32}$$

where $\vec{b}^k$ is the composition of the solid particles created in the kth step.

A comparison of Tables II and III shows that calculations done under the two diffusion limits give very similar results. For example, the abundance differences between these two calculations are generally much smaller than between either calculation and the results of HBB. Therefore, we conclude that the error introduced into our calculation by assuming instantaneous diffusion rather than the actual diffusion rate (whatever that may be) is small. Note that even though the rate of diffusion has very little effect on the average composition in the solid, it has a strong effect on the how that composition varies locally. For sufficiently low diffusion rates, lamellar sheets or other structures may form in the solid (see, e.g., Ref. [32]); these structures can have a strong effect on the thermal conductivity and strength of the crust.

A comparison of Tables II and III to Table I shows that the semianalytic calculation does quite well at reproducing the results of the HBB numerical simulation. All of the abundances from the semianalytic calculation are with 65% of the HBB values and most are significantly closer. Also, many of the table entries that match poorly between the two works correspond to chemical elements with very low abundances, i.e., those elements that are most affected by the finite size of the simulation. For example, the two entries that match the worst between Tables I and II, the solid abundances of elements $Z=10$ and 15, are represented in the simulation by only 58 and 11 ions, respectively.

Figures 2 and 3 provide further comparison of our results and those of HBB. Figure 2 (cf. Fig. 2 of HBB) presents in graphical form the data from Tables I and II, i.e., the final

TABLE III. As in Table II, except that diffusion is assumed to be negligible in the solid (see text).

No diffusion $\langle Z\rangle_l$=27.370, $\langle Z\rangle_s$=30.680, Γ_1=27.38, Γ_l=221.2, Γ_s=260.6 (Γ_1 error: −1%)					
Z	Initial	Liquid	% Error	Solid	% Error
8	0.0301	0.0526	−0.5	0.0076	−13
10	0.0116	0.0204	−0.5	0.0028	+34
12	0.0023	0.0041	−5	0.0005	−14
14	0.0023	0.0041	−4	0.0005	−5
15	0.0023	0.0041	−4	0.0005	+19
20	0.0046	0.0077	+39	0.0015	−47
22	0.0810	0.1289	+26	0.0331	−46
24	0.0718	0.1018	+25	0.0418	−34
26	0.1019	0.1240	+16	0.0798	−22
27	0.0023	0.0025	+1	0.0021	−23
28	0.0764	0.0786	+6	0.0742	−0.5
30	0.0856	0.0753	−3	0.0959	+1
32	0.0116	0.0091	−8	0.0141	+8
33	0.1250	0.0953	−12	0.1547	+11
34	0.3866	0.2863	−16	0.4869	+13
36	0.0023	0.0017	−18	0.0029	−4
47	0.0023	0.0034	+15	0.0012	−11

compositions of the liquid and solid states for both the HBB numerical simulation and our semianalytic calculation. Figure 3 (cf. Fig. 6 of HBB) shows the ratio of the solid abundance to the liquid abundance versus atomic number Z for both works.

Also plotted in Fig. 3 are the abundance ratios in the two-component approximation. In this approximation, the abundance ratios for each element are calculated assuming the plasma is composed of only two ion species, the element itself, and the most abundant element in the mixture (i.e., i =15 or Z=34; see Table I). The initial composition of the mixture is chosen such that the ratio of the abundances of the two elements is the same as in HBB (e.g., x_1/x_{15} =0.0301/0.3866, but now $x_1+x_{15}=1$); however, the results do not change much qualitatively if we choose some other scheme. As with the 17-component plasma, we solve for the point where half of the plasma is liquid and half is solid. Note that the Z=34 abundance ratio is not plotted in Fig. 3 for this approximation, as its value is different for each two-element pairing. The two-component approximation reproduces the abundance ratio trend of the 17-component plasma, including the relatively constant behavior at low Z and the peak at Z=34. It does not give accurate absolute values of the ratios, particularly for Z around Z=34 (where the true solid-to-liquid ratio is greater than unity).

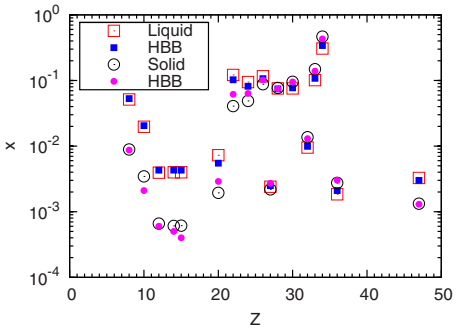

FIG. 2. (Color online) Abundances x as a function of chemical element Z for the final liquid and solid mixtures. Both the values from our equilibrium calculation (Liquid and Solid, large open squares and circles, respectively) and from the numerical simulation of HBB (HBB, small filled squares and circles) are shown.

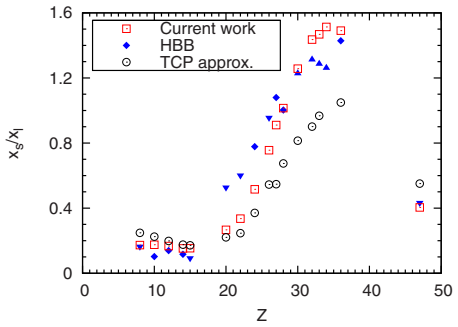

FIG. 3. (Color online) Ratio of the solid abundance to the liquid abundance x_s/x_l as a function of chemical element Z. Both the values from our equilibrium calculation (Current work, open squares) and from the numerical simulation of HBB (HBB, filled diamonds and triangles) are shown, as are the values predicted from the two-component approximation (TCP approx., open circles; see text). If for a given element the HBB ratio is still evolving at the end of the simulation, it is plotted with a triangle that points in the direction of evolution; if the ratio is not changing or is oscillating up and down, it is plotted with a diamond.

The abundances listed in Table I are the compositions of the HBB liquid and solid states at the end of the simulation. These results may not represent the true equilibrium state of the mixture because of the finite run time of the simulation. To show this effect, the HBB abundance ratios are plotted in Fig. 3 using one of three symbols: for a given chemical element, if at the end of the simulation run the ratio is evolving upward in time, it is plotted with an upward-pointing triangle; if the ratio is evolving downward in time, it is plotted with a downward-pointing triangle; and if the ratio is not changing or is oscillating upward and downward, it is plotted with a diamond. The determination of the evolution direction for each element is made using data from the simulation time steps $t_6=t/(10^6\ \mathrm{fm}/c)=71$, 113, and 151, i.e., the last three time steps shown in Fig. 6 of HBB. If the abundance ratio decreases (increases) from $t_6=71$ to 113 and from $t_6=113$ to 151, and the total decrease (increase) across both time intervals is more than 0.1, the ratio is said to be evolving downward (upward) in time; otherwise the ratio is said to be stable. Note that, for the most part, the HBB results are evolving toward the equilibrium values found in our calculation; this behavior is especially apparent for $Z\in[20,34]$, which is also where the abundance ratios differ in the two works by their largest values [37]. This suggests that the errors given in Tables II and III are strong upper limits to the actual accuracy of our calculation.

IV. DISCUSSION

Using results from simulations of one-, two-, and three-component plasmas, we have developed a method for calculating the equilibrium properties of the liquid-solid phase transition in a plasma with an arbitrary number of components in the approximation of a classical ion plasma in a uniform electron background. We used this method to calculate the phase-transition properties for a 17-component plasma with a composition similar to that which might exist in the ocean of an accreting neutron star and compared the results to those of a molecular-dynamics simulation done at the same composition [2]. We found that our method accurately reproduces the results of the HBB simulation. Two sources of error in the simulation may mean that our results represent the actual system even more accurately than this comparison suggests. First, the finite size of the simulation introduces statistical errors which for some components are larger than the discrepancies between the two works. Second, the system is still evolving at the end of the simulation, with many components approaching the values predicted by our calculation.

As in the simulation of HBB, we have followed the 17-component mixture until it reaches the state of 50% liquid and 50% solid. Under these conditions, the term representing the deviation from the linear mixing rule for the solid, Δf_s, is a perturbation on the other terms in the free energy of the solid [see Eq. (24)]. In principle, our calculation can continue to larger fractions of solid, i.e., larger values of the Coulomb coupling parameter Γ. However, because Δf_s increases linearly with Γ and eventually dominates the free energy, the calculation at Γ above the half-freezing point is more sensitive to the form chosen for Δf_s. There is some numerical confirmation of our simple approximation for Δf_s [Eqs. (14) and (25)] for two- and three-component mixtures at large Γ, but only for a very limited set of parameters (see Ref. [15]). Further numerical simulations are necessary to test the validity of these equations at large Γ for general parameters and $(m>3)$-component plasmas.

Another consequence of the large and positive Δf_s term is that for certain compositions, it is energetically favorable for a single solid phase to separate into two or more solid phases (see Sec. II B). Such a phase separation occurs at large Γ in the 17-component plasma simulated by Horowitz *et al.* [19]. With our calculation, we have not yet found any two-solid mixtures that represent the lowest-energy state of the HBB plasma in part because the shape of free-energy surface for the solid phase is very complicated at large Γ. We leave a more careful study of the solid-solid unstable region for future work.

Once these issues are resolved, our calculation will allow the complete phase diagram of multicomponent mixtures to be determined. We expect that these results will have important implications for the structure of the liquid-solid boundary in accreting neutron stars. For example, for an ocean temperature of $T=10^8 T_8$ K, an O-Se mixture with the same proportion of oxygen and selenium as in the HBB mixture (i.e., $\sim 10\%-90\%$) will begin to freeze at a density of $\rho \simeq 2\times 10^7 T_8^3(\mu_e/2)$ g/cm^3, where μ_e is the mean molecular weight per electron. Assuming that accretion is slow enough that the liquid and solid can come into equilibrium at each depth, our phase diagram for a charge ratio $R_Z=34/8$ in Fig. 4 (or Fig. 5) shows that the mixture will reach 50% solid within a factor of 2 in density, but that complete freezing will not occur until much deeper, by a factor of $\simeq(34/8)^5 \simeq 1400$ in density (corresponding to $\rho\simeq 3\times 10^{10} T_8^3$ g/cm^3). This is a very different picture than the sharp transition between liquid and solid expected for a one-component plasma and assumed in previous work on accreting neutron stars. Further work is needed to understand the effects of the various time-dependent processes that are active concurrent with accretion in the ocean-crust transition layer, such as crystallization, diffusion, and sedimentation. For example, sedimentation of the heavier solid particles could be important at low accretion rates, narrowing the transition layer.

ACKNOWLEDGMENTS

We thank Charles Horowitz, Alexander Potekhin, and Don Berry for helpful discussions. This work has been supported in part NSERC and the Canadian Institute for Advanced Research (CIFAR).

APPENDIX A: THE HELMHOLTZ FREE ENERGY VERSUS THE GIBBS FREE ENERGY

Because phase transitions in stars occur at constant pressure, not constant volume, the energy which is at a minimum when the system is in equilibrium is the Gibbs free energy, i.e., $G=F+PV$. We discuss here how our results (Sec. III) change when the Gibbs free energy, rather than the Helm-

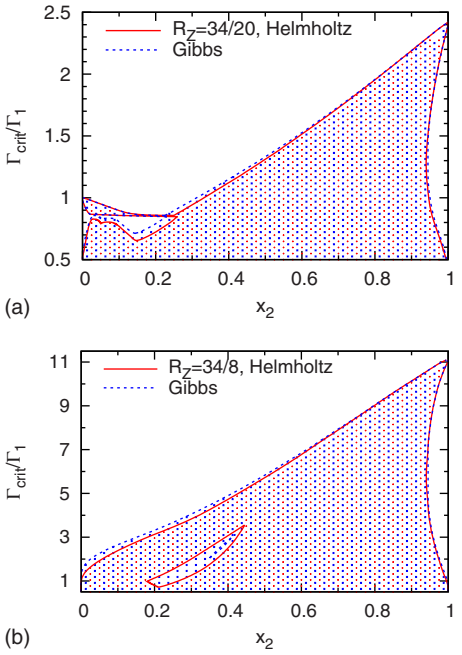

FIG. 4. (Color online) Phase diagrams for charge ratios $R_Z=34/20$ (top panel) and $R_Z=34/8$ (bottom panel). Phase transitions at constant volume are labeled Helmholtz and transitions at constant pressure are labeled Gibbs. To maintain consistency with earlier works (e.g., Refs. [13,15]), Γ_1^{-1} in units of $\Gamma_{\rm crit}^{-1}$ is plotted vs x_2, where $Z_2=34$ for all transitions. The unstable regions are marked by dots. The mixture is liquid for $(x_2,\Gamma_{\rm crit}/\Gamma_1)$ points entirely above the unstable region; for points below any part of the unstable region (such as the peninsula in the bottom-left corner of the top panel and the banana-shaped island in the bottom panel), the mixture is solid.

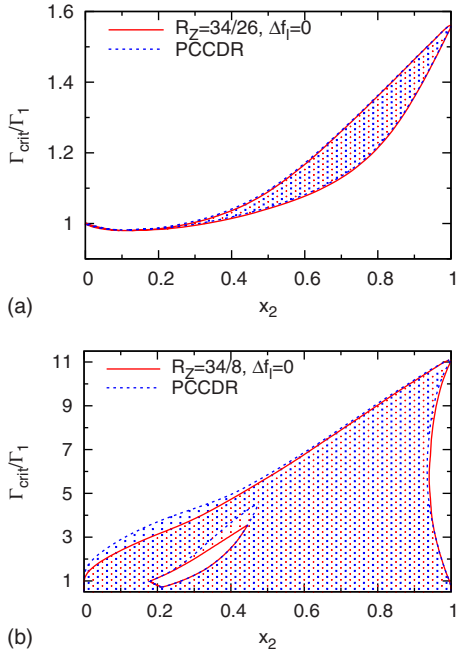

FIG. 5. (Color online) Phase diagrams for charge ratios $R_Z=34/26$ (top panel) and $R_Z=34/8$ (bottom panel). Phase transitions where the liquid deviation term Δf_l is ignored are labeled "$\Delta f_l=0$" and transitions where the liquid deviation is given by Eq. (9) of [35] are labeled PCCDR.

holtz free energy, is used to determine the equilibrium state.

To calculate the Gibbs free energy, we follow the perturbation method of Ogata *et al.* [15], though we ignore terms due to the electron exchange energy (see, e.g., Ref. [33]; these terms are small for highly relativistic plasmas such as are found at the ocean-crust boundaries of accreting neutron stars). In the degenerate interiors of white dwarfs and neutron stars, the electrons make the dominant contribution to the total pressure ($P_i \sim \alpha\langle Z^{2/3}\rangle P_e$ for $\Gamma>1$; see, e.g., Ref. [34]) and so we can treat the ion partial pressures as perturbations.

The Helmholtz free energy of the system is

$$F = F_0 + F_1, \tag{A1}$$

where F_0 is the kinetic energy of the electrons and F_1 is the free energy of the ions (the electron exchange term is ignored and the Coulomb term is folded into the ion free energy). The total pressure of the system is

$$P \equiv -\frac{\partial F}{\partial V} = -\frac{\partial F_0}{\partial V} - \frac{\partial F_1}{\partial V}. \tag{A2}$$

Let V_0 be the volume of the unperturbed system when only electrons contribute to the total pressure; let V_{01} be the volume of the perturbed system when both ions and electrons contribute to the total pressure. Then the total pressure can also be expressed as

$$P = -F_0'(V_0) \tag{A3}$$

and

$$P = P(V_0) + \delta V P'(V_0) + \frac{\delta V^2}{2} P''(V_0) + \cdots, \tag{A4}$$

where $\delta V = V_{01} - V_0$ and we are using the notation $P'(V_0) = [\frac{\partial P}{\partial V}]_{V=V_0}$, etc. From Eqs. (A2)–(A4) and assuming δV is small (which can easily be checked *a posteriori*), we obtain

$$\delta V = -\frac{F_1'(V_0)}{F_0''(V_0)}. \tag{A5}$$

The Gibbs free energy can be written as

$$G = G(V_0) + \delta V G'(V_0) + \frac{\delta V^2}{2} G''(V_0) + \cdots \tag{A6}$$

$$= F_0(V_0) + F_1(V_0) + P(V_0)V_0 + \delta V P'(V_0)V_0 + \frac{\delta V^2}{2} P''(V_0)V_0 + \frac{\delta V^2}{2} P'(V_0) + \cdots \tag{A7}$$

$$= F_0(V_0) + F_1(V_0) + PV_0 - \frac{[F_1'(V_0)]^2}{2F_0''(V_0)}, \tag{A8}$$

where in going from Eq. (A6) to Eq. (A7), we have made use of the thermodynamic relation

$$V \equiv -\frac{\partial G}{\partial P}. \tag{A9}$$

The Gibbs free energy is obtained from Eq. (A8) once the value of V_0 is known. For a given total pressure P, the volume V_0 is determined by Eq. (A3). We have (e.g., Ref. [33])

$$P = -F_0'(V_0) = \frac{m_e c^2}{8\pi^2 \lambda\!\!\!^{-3}_c}\left[y\sqrt{1+y^2}\left(\frac{2y^2}{3} - 1\right) + \ln(y + \sqrt{1+y^2})\right], \tag{A10}$$

where the "relativity parameter"

$$y \equiv \frac{p_F}{m_e c} = \lambda\!\!\!^{-}_c (3\pi^2 n_e)^{1/3} = \left(\frac{9\pi}{4}\right)^{1/3} \frac{k_B T}{\alpha m_e c^2}\Gamma_e \tag{A11}$$

is evaluated at $V=V_0$. Here, $\alpha=e^2/(\hbar c)$ is the fine-structure constant and $\lambda\!\!\!^{-}_c=\hbar/(m_e c)$ is the reduced Compton wavelength. The volume V_0 depends only on the total pressure of the system and so is the same for both the liquid and solid states. The Helmholtz free energy in the unperturbed state, $F_0(V_0)$, is also the same for both states. We can therefore ignore the $F_0(V_0)$ and PV_0 terms in Eq. (A8) when calculating the state of lowest free energy. Using

$$F_0''(V_0) = \frac{1}{V_0}\frac{m_e c^2}{9\pi^2 \lambda\!\!\!^{-3}_c}\frac{y^5}{\sqrt{1+y^2}}, \tag{A12}$$

we arrive at our final expression for the Gibbs free energy of the liquid ($i=l$) or solid ($i=s$) state

$$g_i \equiv \frac{G_i}{N k_B T} = f_i(\Gamma_e) - \frac{\alpha}{3(18\pi)^{1/3}\langle Z\rangle}\frac{\sqrt{1+y^2}}{y}\Gamma_e\left[\frac{\partial f_i}{\partial \Gamma_e}\right]^2, \tag{A13}$$

where f_i is the Helmholtz free energy given in Secs. II A–II C, $y(P)$ is found from Eq. (A10), and $\Gamma_e(y)$ is found from Eq. (A11) (i.e., Γ_e is evaluated at $V=V_0$).

We calculate the phase diagrams for two-component plasmas with charge ratios $R_Z=Z_2/Z_1$ up to 34/8, first using the relevant expressions for f_l and f_s from Sec. II B (i.e., ignoring pressure terms) and then using Eq. (A13) (including pressure terms). Note that the Γ_e values in Eq. (A13) are evaluated at $V=V_0$, while those in Sec. II B are evaluated at $\simeq V_{01}$. In order to show the two sets of phase diagrams on the same axis, we use the relation [cf. Eq. (A5)]

$$\Gamma_e(V_{01}) = \Gamma_e(V_0)\left(\frac{V_{01}}{V_0}\right)^{1/3} = \Gamma_e(V_0)\left[1 + \frac{2\alpha}{(18\pi)^{1/3}\langle Z\rangle}\frac{\sqrt{1+y^2}}{y}\frac{\partial f_l}{\partial \Gamma_e}\right]^{1/3}, \tag{A14}$$

where all instances of y and Γ_e on the right-hand side of Eq. (A14) are evaluated at $V=V_0$. Here, we choose to solve for $\Gamma_e(V_{01})$ of the liquid, although the results are practically the same if $\Gamma_e(V_{01})$ of the solid is used instead (since the two Γ_e values differ by at most 0.004% even for $R_Z\simeq 4$). Our results, plotted as a function of $\Gamma_1(V_{01})=Z_1^{5/3}\Gamma_e(V_{01})$, are shown in Fig. 4. Not surprisingly, we obtain results very similar to those found by [15]: the assumption of transitions at constant volume rather than at constant pressure has no effect on the phase diagram unless $R_Z \gtrsim 2$, in which case the only effect is to widen the unstable region slightly. For $2 < R_Z < 5$, the unstable region widens by at most 1%–2%, with the largest change occurring for $\Gamma_1 \lesssim \Gamma_{\rm crit}$. Since the calculation of Sec. III was done at a relatively low value of Γ (at $\Gamma_{Z=8}\simeq 27$, which is below $\Gamma_{\rm crit}$ for all species $Z<25$), we expect that the results shown there will not change when the Gibbs free energy is used. At large Γ, however, when nearly all of the mixture is in the solid state (see Sec. IV), inclusion of the Gibbs free energy in the equations of Sec. II C may be necessary to accurately determine the phase-transition properties under these conditions.

APPENDIX B: THE DEVIATION FROM LINEAR MIXING IN THE LIQUID

In our calculation, we assume perfect linear mixing in the liquid state by setting $\Delta f_l=0$. We discuss here how our results (Sec. III) change when a more accurate form for Δf_l is used.

There are several fitting formulas of Δf_l available in the literature (e.g., Refs. [15,18,35]). We choose to implement the fit from Eq. (9) of Potekhin *et al.* [35] (hereafter PCCDR), since it provides accurate results for Δf_l over a wide range of Γ values, Z ratios, and fractional abundances of each species. It is also the only fit we are aware of that is immediately applicable to plasmas with more than two components, though we do not make use of that feature here.

We calculate the phase diagrams for two-component plasmas with charge ratios R_Z up to 34/8, first for $\Delta f_l=0$ and then using Eq. (9) of PCCDR (i.e., for $\Delta f_l \neq 0$). Our results are shown in Fig. 5. We find that the assumption $\Delta f_l=0$ has no effect on the phase diagram unless $R_Z \gtrsim 3$, in which case the only effect is to shift the low-x_2 side (left side in Fig. 5) of the unstable region toward even smaller values of x_2. The shift is most significant for large R_Z and Γ, with shifts of around 5% of the width of the unstable region for $R_Z\simeq 4$ and $\Gamma_1 \simeq \Gamma_{\rm crit}$. Since our calculation was done at a relatively low value of Γ, we expect that the results of Sec. III will not change when an accurate form for Δf_l is used (cf. Appendix A). At larger values of Γ, a Δf_l term may be necessary to ensure the accuracy of the calculation.

Here and in Appendix A, we have compared phase diagrams generated by our calculation to those that are generated if additional terms are considered. We can also compare our phase diagrams to those of other works. Particular fruitful comparisons can be made with Segretain and Chabrier [13] and Ogata *et al.* [15], since these works present phase diagrams at several different values of R_Z; the R_Z values in Figs. 4 and 5 were chosen in part because of the similarity to the ratios presented in these two works (i.e., $R_Z=34/26 \simeq 4/3=1/0.75$, $R_Z=34/20\simeq 5/3\simeq 1/0.55$, and $R_Z=34/8 \simeq 13/3$). Our diagrams agree closely with those of [15], with one important exception: for most values of R_Z, this group finds "azeotropic points" or eutectic points at $x_2 \lesssim 0.04$ that do not exist in our diagrams. The close agreement for

$x_2 > 0.04$ is due to the fact that both our group and theirs used fitting formulas with the same form for Δf_s [Eq. (13)], while the poor agreement at $x_2 < 0.04$ is due to the fact that we used $\Delta f_l = 0$ while [15] used a form for Δf_l that was negative for $x_2 \lesssim 0.05$. Our diagrams agree less closely with those of [13], though the agreement is still very good at small Γ (in the upper half of each diagram). Even at large Γ, the diagrams of our group and theirs are qualitatively similar, with the main differences being the larger amount of stable solid regions at high x_2 and the delayed (in terms of increasing R_Z) transition from spindle type to azeotropic type in the diagrams of [13]. We find that the transition from spindle-type to azeotropic-type phase diagrams occurs at $R_Z \simeq 1.2 \simeq 28/34 \simeq 1/0.83$, which is a somewhat lower value of R_Z than found by Segretain and Chabrier [13] or DeWitt *et al.* [18] $(1/0.72 \simeq 1.4)$.

APPENDIX C: THE DEVIATION FROM LINEAR MIXING IN THE SOLID

In this section, we provide a simple estimate of Δf_s for multicomponent plasmas using the approximation that only nearest neighbors contribute to the interaction energy of each ion (see, e.g., Ref. [32]). The expression found here is too simplistic for use in our calculation, but illustrates the general form of Δf_s for plasmas with three or more components; the Δf_s term of Sec. II [Eq. (25)] has a very similar form.

Let $u_{ij} = U_{ij}/(N k_B T)$ be the interaction energy between nearest-neighbor ions of species i and j $(u_{ij} = u_{ji})$. When all ion species are completely separated, the interaction energy per ion for species i is $u_{ii}/2$ and the total interaction energy of the system is given by

$$u_{\rm sep} = \frac{1}{2} \sum x_i u_{ii}. \tag{C1}$$

When the ion species are mixed, the interaction energy per ion for species i is $\Sigma_j x_j u_{ij}/2$, assuming that the various ions are randomly distributed throughout the mixture. The total energy of the system is then

$$u_{\rm mix} = \frac{1}{2} \sum_i \sum_j x_i x_j u_{ij}. \tag{C2}$$

The internal energy of mixing for the solid, $\Delta u_s = u_{\rm mix} - u_{\rm sep}$, is given by

$$\Delta u_s = \frac{1}{2} \sum_i x_i \left(\sum_j x_j u_{ij} - u_{ii} \right)$$

$$= \frac{1}{2} \sum_i x_i \sum_{j \neq i} x_j (u_{ij} - u_{ii}) = \sum_i \sum_{j>i} x_i x_j \left(u_{ij} - \frac{u_{ii} + u_{jj}}{2} \right). \tag{C3}$$

The free energy of mixing can be found from the thermodynamic identity

$$f = \int_0^\beta \frac{u(\beta')}{\beta'} d\beta', \tag{C4}$$

where $\beta = 1/(k_B T)$ (see, e.g., Ref. [10]). Assuming that the interaction energies u_{ij} scale linearly with β (which is true, e.g., if $u_{ij} \propto \Gamma_e$), we have

$$\Delta f_s = \sum_i \sum_{j>i} x_i x_j \left(u_{ij} - \frac{u_{ii} + u_{jj}}{2} \right), \tag{C5}$$

which of the same form as Eq. (25).

[1] B. M. S. Hansen and J. Liebert, Annu. Rev. Astron. Astrophys. **41**, 465 (2003).
[2] C. J. Horowitz, D. K. Berry, and E. F. Brown, Phys. Rev. E **75**, 066101 (2007).
[3] J. Isern, R. Mochkovitch, E. García-Berro, and M. Hernanz, Astron. Astrophys. **241**, L29 (1991).
[4] H. Schatz, A. Aprahamian, V. Barnard, L. Bildsten, A. Cumming, M. Ouellette, T. Rauscher, F. Thielemann, and M. Wiescher, Nucl. Phys. A **688**, 150 (2001).
[5] S. Gupta, E. F. Brown, H. Schatz, P. Möller, and K. Kratz, Astrophys. J. **662**, 1188 (2007).
[6] C. J. Horowitz and D. K. Berry, Phys. Rev. C **79**, 065803 (2009).
[7] P. S. Shternin, D. G. Yakovlev, P. Haensel, and A. Y. Potekhin, Mon. Not. R. Astron. Soc. **382**, L43 (2007).
[8] E. F. Brown and A. Cumming, Astrophys. J. **698**, 1020 (2009).
[9] C. J. Horowitz and K. Kadau, Phys. Rev. Lett. **102**, 191102 (2009).
[10] A. Y. Potekhin and G. Chabrier, Phys. Rev. E **62**, 8554 (2000).
[11] R. Mochkovitch, Astron. Astrophys. **122**, 212 (1983).
[12] J. L. Barrat, J. P. Hansen, and R. Mochkovitch, Astron. Astrophys. **199**, L15 (1988).
[13] L. Segretain and G. Chabrier, Astron. Astrophys. **271**, L13 (1993).
[14] L. Segretain, Astron. Astrophys. **310**, 485 (1996).
[15] S. Ogata, H. Iyetomi, S. Ichimaru, and H. M. Van Horn, Phys. Rev. E **48**, 1344 (1993).
[16] H. DeWitt and W. Slattery, Contrib. Plasma Phys. **43**, 279 (2003).
[17] H. Iyetomi, S. Ogata, and S. Ichimaru, Phys. Rev. B **40**, 309 (1989).
[18] H. DeWitt, W. Slattery, and G. Chabrier, Physica B **228**, 21 (1996).
[19] C. J. Horowitz, O. L. Caballero, and D. K. Berry, Phys. Rev. E **79**, 026103 (2009).
[20] G. S. Stringfellow, H. E. DeWitt, and W. L. Slattery, Phys. Rev. A **41**, 1105 (1990).
[21] S. Ogata and S. Ichimaru, Phys. Rev. A **36**, 5451 (1987).
[22] J. M. Caillol, J. Chem. Phys. **111**, 6538 (1999).
[23] J. P. Hansen, Phys. Rev. A **8**, 3096 (1973).
[24] R. T. Farouki and S. Hamaguchi, Phys. Rev. E **47**, 4330 (1993).
[25] D. H. E. Dubin, Phys. Rev. A **42**, 4972 (1990).
[26] W. L. Slattery, G. D. Doolen, and H. E. DeWitt, Phys. Rev. A

26, 2255 (1982).
[27] E. L. Pollock and J. P. Hansen, Phys. Rev. A **8**, 3110 (1973).
[28] S. Ichimaru, H. Iyetomi, and S. Tanaka, Phys. Rep. **149**, 91 (1987).
[29] H. Iyetomi and S. Ichimaru, Phys. Rev. A **27**, 3241 (1983).
[30] H. Iyetomi, S. Ogata, and S. Ichimaru, Phys. Rev. A **46**, 1051 (1992).
[31] A. Y. Potekhin, G. Chabrier, and F. J. Rogers, Phys. Rev. E **79**, 016411 (2009).
[32] P. Gordon, *Principles of Phase Diagrams in Materials Systems* (McGraw-Hill, New York, 1968).
[33] E. E. Salpeter, Astrophys. J. **134**, 669 (1961).
[34] *Neutron Stars 1: Equation of State and Structure*, edited by P. Haensel, A. Y. Potekhin, and D. G. Yakovlev, Astrophysics and Space Science Library Vol. 326 (Springer, New York, 2007).
[35] A. Y. Potekhin, G. Chabrier, A. I. Chugunov, H. E. DeWitt, and F. J. Rogers, Phys. Rev. E **80**, 047401 (2009).
[36] In both calculations, we assume that the liquid diffusion is rapid. This is usually the case for terrestrial mixtures undergoing phase transitions (e.g., Ref. [32]), but it appears to be true for the ocean of an accreting neutron star as well [C. Horowitz (private communication)].
[37] After their work was published, HBB ran their simulation an additional 208×10^6 fm/c to a total simulation time of 359×10^6 fm/c. Of the solid-to-liquid abundance ratios that were still evolving at the time of the HBB publication (i.e., those presented with upward- or downward-pointing triangles in our Fig. 3), by 359×10^6 fm/c, just over half had evolved closer to our results ($Z=15$, 20, 22, 30, 32, and 34), while the rest either had remained steady ($Z=8$) or had evolved farther away ($Z=26$, 33, and 47) [D. Berry (private communication)].